Three-Dimensional Analysis of Molten Pool in GMA-Laser Hybrid Welding

Analytical models of GMA and laser keyhole welding are merged to achieve the simulation of hybrid welding considering the multiple reflections of laser and the Fresnel absorption theory

BY J.-H. CHO AND S.-J. NA

ABSTRACT

A computational analysis of a molten pool in laser-GMA hybrid welding is achieved including free-surface tracking using the well-known volume of fluid (VOF) method. The suggested three-dimensional transient numerical model includes all known analytical key features of arc welding including electromagnetic force, buoyancy, and arc pressure. In addition to the basic GTA model, molten droplets are artificially generated and allowed to fall down to the pool to cover the GMAW process. A keyhole analysis model is merged to a GMAW simulation model with the assumption that the interaction between the laser and the arc is negligible for convenience. The keyhole model is established on a unique phenomena that includes multiple reflections, Fresnel absorption model, and the recoil pressure in laser welding apart from the inverse Bremsstrahlung absorption. The result shows the flow patterns of the molten pool in GMA-laser hybrid welding, and they are compared to previously reported observation results. The molten flow at the bottom of the keyhole rises up slowly, and therefore a vortex can be observed throughout the molten pool. However, the flow pattern became increasingly complicated. The flow of the keyhole root is split into three main streams, and one stream is continuously maintained in the vortex.

J.-H. CHO and S.-J. NA (sjna@kaist.ac.kr) *are with Department of Mechanical Engineering, Korea Advance Institute of Science and Technology, Yuseong-gu, Daejeon, Republic of Korea.*

Introduction

Welding is a complex multiphysics topic related to plasma physics, electro magnetism, and fluid dynamics including metallurgy. In addition, it is impossible to observe the welding process directly because the pool and arc plasma are very bright, and their temperatures are exceedingly high. Therefore, various types of research have been reported to monitor the welding process. A representative method is the checking of the current or voltage of gas tungsten arc (GTA) or gas metal arc (GMA) welding (Refs. 1–3). There are more sophisticated methods that directly record the pool images using a CCD camera or that use such a camera combined with optical filters and various light sources such as specific laser or halogen lamps (Refs. 4, 5). However, all of the aforementioned techniques are indirect techniques; specifically, they do not provide any information concerning the phenomena occurring inside the weld pool. In other words, they merely present the predictability of bead shapes, resulting in a lack of scientific information regarding the flow and related phenomena.

An impressive method that enables the pool to be observed directly is a real-time X-ray imaging system (Refs. 6, 7). X-rays transmitted through the workpiece in a laser keyhole welding process are focused on a CCD camera and are then reconstructed as gray-scaled images in real time. It is very useful to see the keyhole and pores instantaneously in the weldment during the process, as it is possible to monitor the bead formation process. In spite of these advantages, it is difficult to construct the system in the actual production area, as it is expensive compared to conventional monitoring methods. Additionally, there are concerns regarding health problems related to radiation. Furthermore, the information available through this system remains insufficient if one wishes to comprehend the physical meanings of the welding process. The achieved images are two-dimensional, gray-scaled, and comparatively rough, making it difficult to understand the details of the flow in the X-ray images.

In this area, computer simulations can greatly facilitate the comprehension of molten pool dynamics. Although the analysis of a molten pool based on computational fluid dynamics is not a complete answer to the questions regarding heat and mass transfer problems in the welding process, it provides a passable answer. Simulation results show the flow of the molten pool and the formation of the weldment as well as its historical temperature profile. Hence, a number of studies regarding weld pool analysis have been reported since the 1980s.

In early simulations of arc welding, it was impossible to accomplish a flow analysis of molten metal that included free-surface tracking (Refs. 8, 9). However, due to advances in computer and numerical techniques, knowledge of the total flow patterns of the molten pool have been achieved that include the expression of the free surface (Refs. 10, 11), as well as the inclusion of droplets via a feeding wire (Refs. 12, 13).

For keyhole dynamics in the laser welding process, a geometrically assumed keyhole such as a cylindrical hole in a plate was typically used to analyze the effects in early studies that did not incorporate the expression of the free surface of molten material, as mentioned above (Ref. 14). Currently, keyhole dynamics

KEYWORDS

Gas Metal Arc Welding (GMAW)
Laser
Hybrid Welding
Volume of Fluid (VOF)
Keyhole
Fresnel

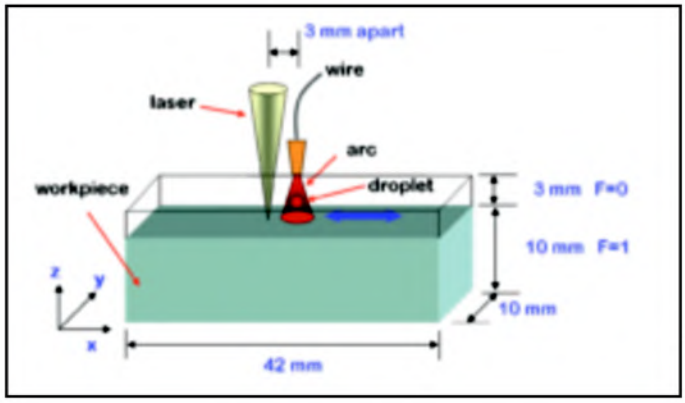

Fig. 1 — Schematic diagram of laser-GMA hybrid welding simulation.

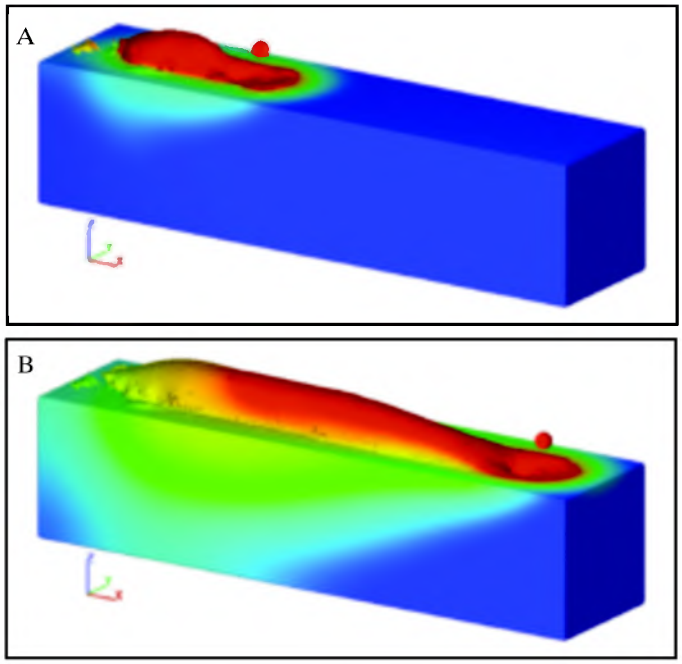

Fig. 2 — 3-D perspective views of simulation results. A — t=0.45 s; B — t= 1.8 s.

including the evolutionary free-surface shape achieved by VOF (Ref. 15) or the level-set method are typically reported (Refs. 16, 17). One of the most important features of keyhole simulation is the multiple reflection effect. If the laser beam is considered as a bundle of rays, it can be easily understood that each of the rays travels inside the keyhole through multiple reflections at the keyhole wall until it escapes out of it. Therefore, the ray tracing profile inside the keyhole is entirely dependent on the external shape of the keyhole, which means the keyhole surface exposed to laser rays (Ref. 18). Consequently, the exact keyhole profile and a ray tracing algorithm are needed for every single time step in a simulation in order to obtain a precise energy distribution map of the keyhole surface.

In this paper, the analysis of a three-dimensional molten pool analysis is achieved for a laser-GMA hybrid welding process. Analytical models for GMA and laser keyhole welding are merged to realize the hybrid welding process in a computer simulation. A real-time ray tracing technique (Ref. 23) that takes into account a discrete grid cell in the VOF method is adopted to realize a multiple reflection effect for every time step according to the present keyhole profile. There are several assumptions and simplifications used in the analysis. First, it is assumed that the arc plasma and the laser do not interact; consequently, they are only mathematically superposed in the simulation. Secondly, both the arc and the laser are considered as surface heat flux with a Gaussian distribution. Lastly, the effect of shielding gas is not considered in the analysis. The simulation was conducted using the commercial package Flow3D. Suggested analytical model is already validated by comparing the simulation result to the experiment (Refs. 23, 24).

Molten Pool Dynamics

To execute the molten pool analysis, three governing equations are essential, as with other normal fluidic problems. They are the continuity equation, the momentum equation, which here is referred to as the Navier-Stokes equation, and the energy equation. The metallic fluid in this simulation is assumed as incompressible, laminar, and Newtonian.

Based on these assumptions, the governing equations are expressed as follows. First, the continuity equation (Ref. 19), implies that the conservation of the material has the form shown in Equation 1.

$$\frac{\partial}{\partial x}\left(uA_x\right)+\frac{\partial}{\partial y}\left(vA_y\right)+\frac{\partial}{\partial z}\left(wA_z\right)=0 \qquad (1)$$

In Equation 1, u, v, and w denote the velocity component according to each axis in the Cartesian coordinates. A_x, A_y, and A_z denote the fractional area open to the flow in each direction. t is the time, and ρ, P, μ, and G_z denote the density, pressure, viscosity, and gravitational acceleration in the momentum equation, respectively. They can be expressed as follows:

$$\frac{\partial u}{\partial t}+\frac{1}{V_F}\left\{uA_x\frac{\partial u}{\partial x}+vA_y\frac{\partial u}{\partial y}+wA_z\frac{\partial u}{\partial z}\right\} =-\frac{1}{\rho}\frac{\partial p}{\partial x}+f_x \qquad (2)$$

$$\frac{\partial v}{\partial t}+\frac{1}{V_F}\left\{uA_x\frac{\partial v}{\partial x}+vA_y\frac{\partial v}{\partial y}+wA_z\frac{\partial v}{\partial z}\right\} =-\frac{1}{\rho}\frac{\partial p}{\partial y}+f_y \qquad (3)$$

$$\frac{\partial w}{\partial t}+\frac{1}{V_F}\left\{uA_x\frac{\partial w}{\partial x}+vA_y\frac{\partial w}{\partial y}+wA_z\frac{\partial w}{\partial z}\right\} =-\frac{1}{\rho}\frac{\partial p}{\partial z}+f_z+G_z \qquad (4)$$

Here, V_F denotes the volume fraction in the cell in the VOF method (Ref. 20) and f_x, f_y, and f_z indicate the viscous acceleration rates as in Equations 5–7.

$$f_x=-\frac{1}{\rho V_F}\left\{\begin{array}{l}\dfrac{\partial}{\partial x}\left(A_x\tau_{xx}\right)+\dfrac{\partial}{\partial y}\left(A_y\tau_{xy}\right)\\ +\dfrac{\partial}{\partial z}\left(A_z\tau_{xz}\right)\end{array}\right\} \qquad (5)$$

$$f_y=-\frac{1}{\rho V_F}\left\{\begin{array}{l}\dfrac{\partial}{\partial x}\left(A_x\tau_{xy}\right)+\dfrac{\partial}{\partial y}\left(A_y\tau_{yy}\right)\\ +\dfrac{\partial}{\partial z}\left(A_z\tau_{yz}\right)\end{array}\right\} \qquad (6)$$

$$f_z=-\frac{1}{\rho V_F}\left\{\begin{array}{l}\dfrac{\partial}{\partial x}\left(A_x\tau_{xz}\right)+\dfrac{\partial}{\partial y}\left(A_y\tau_{yz}\right)\\ +\dfrac{\partial}{\partial z}\left(A_z\tau_{zz}\right)\end{array}\right\} \qquad (7)$$

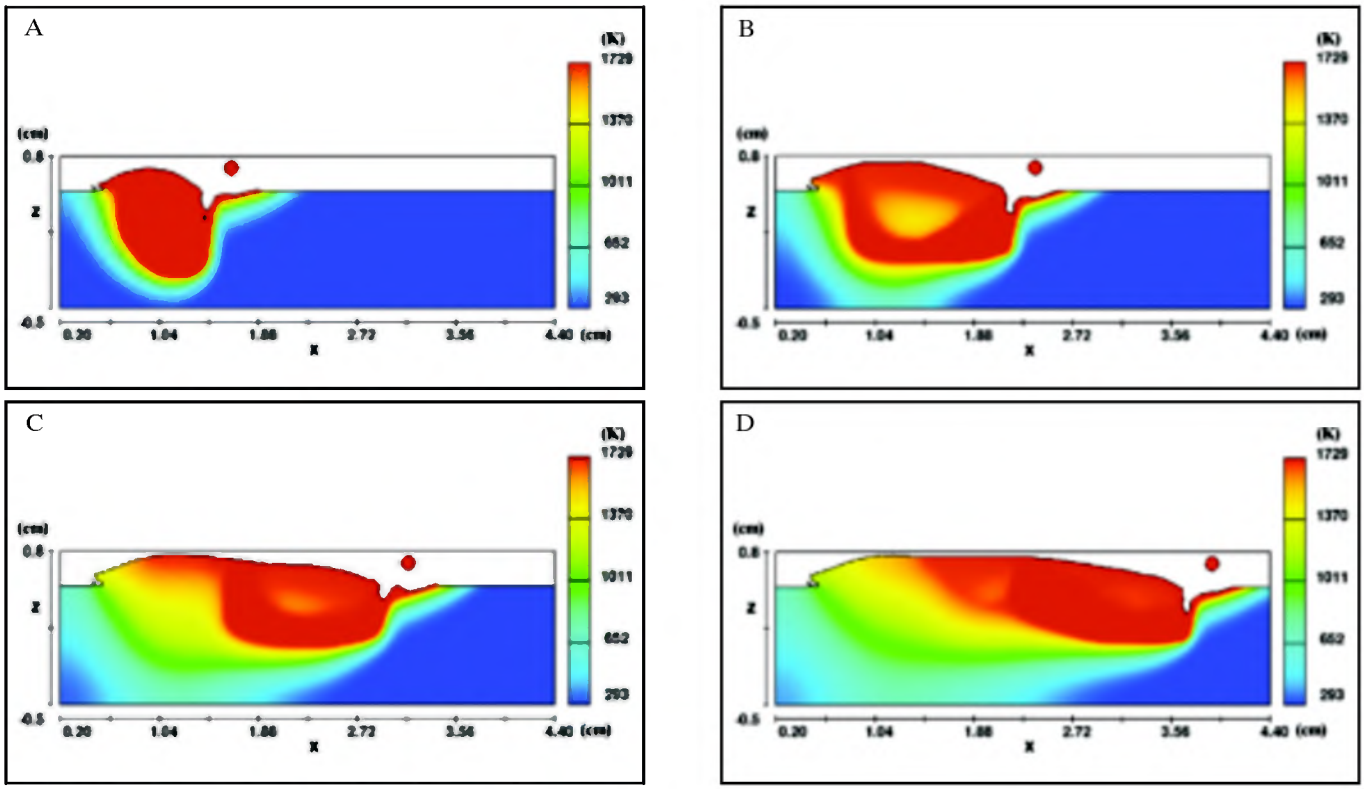

Fig. 3 — Temperature profiles of cross-sectioned side views in the simulation result. A — t=0.45 s; B — t=0.9 s; C — t=1.35 s; D — t=1.8 s.

Where

$$\tau_{xx} = -2\mu\left\{\frac{\partial u}{\partial x} - \frac{1}{3}\left(\frac{\partial u}{\partial x} + \frac{\partial v}{\partial y} + \frac{\partial w}{\partial z}\right)\right\},$$

$$\tau_{yy} = -2\mu\left\{\frac{\partial v}{\partial y} - \frac{1}{3}\left(\frac{\partial u}{\partial x} + \frac{\partial v}{\partial y} + \frac{\partial w}{\partial z}\right)\right\},$$

$$\tau_{zz} = -2\mu\left\{\frac{\partial w}{\partial z} - \frac{1}{3}\left(\frac{\partial u}{\partial x} + \frac{\partial v}{\partial y} + \frac{\partial w}{\partial z}\right)\right\},$$

$$\tau_{xy} = -\mu\left\{\frac{\partial v}{\partial x} + \frac{\partial u}{\partial y}\right\},\ \tau_{xz} = -\mu\left\{\frac{\partial u}{\partial z} + \frac{\partial w}{\partial x}\right\},$$

$$\tau_{yz} = -\mu\left\{\frac{\partial v}{\partial z} + \frac{\partial w}{\partial y}\right\} \quad (8)$$

Additionally, the energy equation based on the enthalpy method and the continuum formulation is described below.

$$\frac{\partial h}{\partial t} + \left(\vec{V}\cdot\nabla\right)h = \rho\nabla\cdot\left(K\nabla T\right) \quad (9)$$

$$h = C_p \cdot T + f \cdot L_f \quad (10)$$

Where f denotes

$$f\left(T\right) = \begin{cases} 0, \text{ if } T \le T_S \\ \dfrac{T - T_L}{T_L - T_S}, \text{ if } T_S < T < T_L \\ 1, \text{ if } T \ge T_L \end{cases} \quad (11)$$

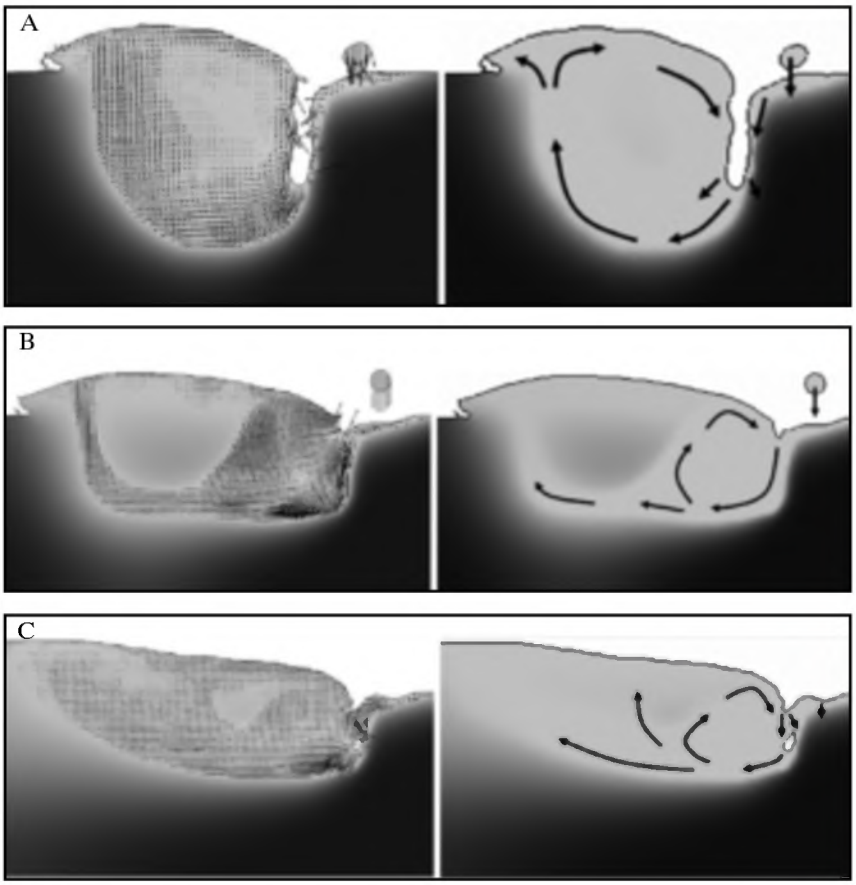

Fig. 4 — Flow patterns of simulation result in cross-sectional side views. A — t=0.53 s; B — t=0.99 s; C — t=1.96 s.

In this equation, h and K indicate the enthalpy and the thermal conductivity, respectively, and T, T_L, and T_S, correspondingly, denote the temperature, liquidus temperature, and solidus temperature.

In terms of the energy transfer, the laser beam is a type of complex heat source model that interacts with various materials. However, it is generally treated as a surface heat flux boundary condition in an analysis, and there is a widely accepted simple expression in the form of a Gaussian function related to the TEM_{00} mode in laser activity with a mathematical form as in the following equation (Ref. 21):

$$q_L\left(x,y,z\right)=\frac{3Q}{\pi r_L^2}\exp\left(-3\frac{x^2+y^2}{r_L^2}\right) \quad (12)$$

$$r_L=r_0+a\left|z_0-z\right| \quad (13)$$

In Equation 12, Q indicates the nominal laser power and the coefficient 3 indicates that 95% of the total power exists inside the area of the effective radius r_L. Particularly, the laser beam is modeled to have a diverging property along the traveling path in this research. This is more realistic than earlier models of a collimated beam. Therefore, the beam model becomes a three-dimensional function by appending Equation 13 to Equation 12. The beam radius is set so as to increase linearly along the path, with a focal radius r_0 at the z_0 position in the z axis.

The electric arc is modeled as a type of surface heat flux with a Gaussian distribution shape. Its mathematical form is, therefore, similar to that of Equation 12 exclusive of the diverging effective radius, which is changed to a fixed radius as in the following:

$$q_A\left(x,y\right)=\frac{VI}{2\pi r_A^2}\exp\left(-\frac{x^2+y^2}{2r_A^2}\right) \quad (14)$$

Here, V and I are the voltage and current of the arc, respectively, and r_A is the fixed effective radius of the arc. It is equal to 3 mm. In contrast to the equation of the laser heat source, this equation is a two-dimensional function. Thus, its shape remains unchanged along the z axis.

After achieving the heat source models, the pressure boundary conditions must be confirmed. In an arc welding process, the pool experiences a small deformation along its top surface due to the arc pressure caused by the massive flow of arc plasma; this has the form of a Gaussian distribution as in the following equation (Ref. 15):

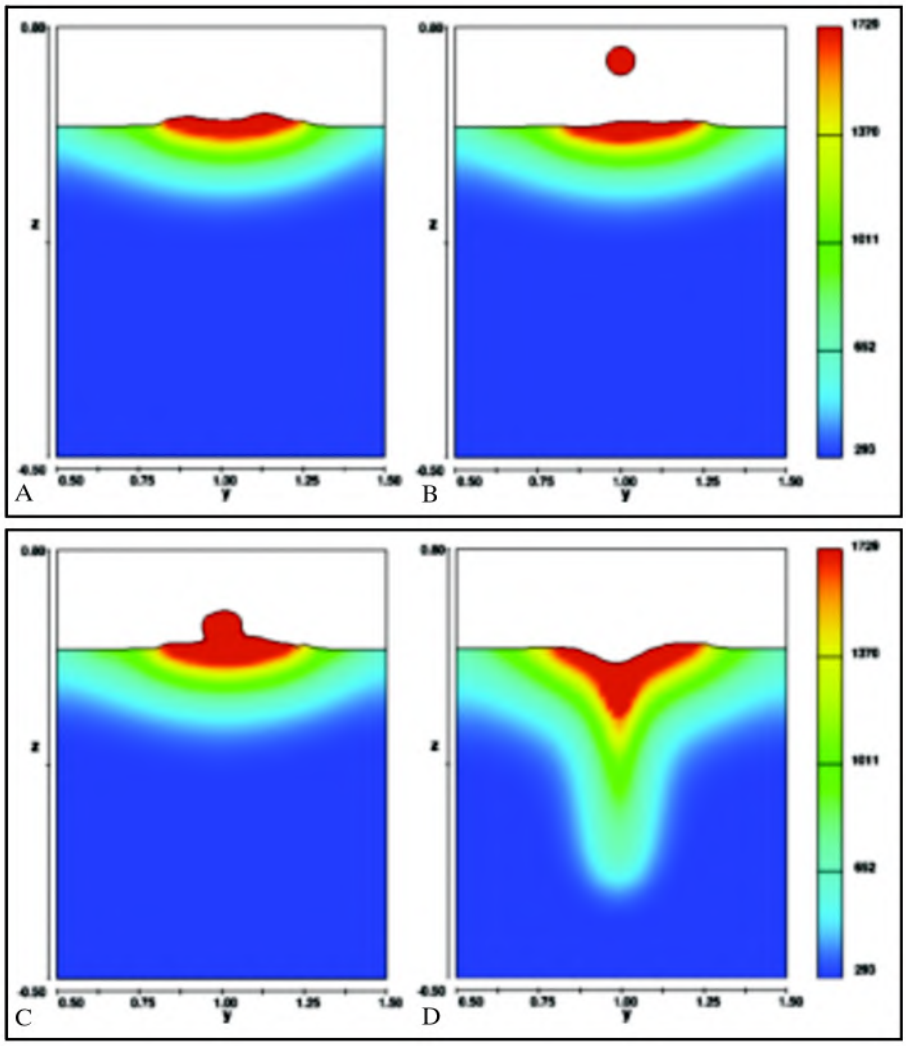

Table 1 — Material Properties and Coefficients Used in Analysis

Properties	Value
Density	7490 kg/m^3
Thermal conductivity	35 W/mK
Specific heat	606 J/kgK
Latent heat of vaporization	6084 kJ/kg
Latent heat of fusion	260 kJ/kg
Liquidus temperature	1787.5 K
Solidus temperature	1729.2 K
Liquid-vapor equlibrium temperature	3130 K
Magnetic permeability	1.26e–6 H/m
Viscosity	0.006 kg/ms
Thermal expansion rate	4.2×10^{-5}/K
Surface tension	1.2 N/m
Surface tension gradient	-0.2×10^{-3} N/mK
Focal radius, r_0	0.25 mm
Beam divergence in Equation 13, a	0.2
Universal gas constant	8.314 J/molK

$$P_A\cong\frac{\mu_0 I^2}{4\pi^2 r_A^2}\exp\left(-\frac{r^2}{2r_A^2}\right) \quad (15)$$

For a laser beam welding case, the pressure boundary condition is entirely different from Equation 15. Deformation of the surface mainly depends on the evaporation of material in a process referred to as the recoil pressure, which is the main driving force in the creation of a keyhole. A precise mathematical model for this phenomenon does not exist, but the Equation 16 reported in 2002 is simple and can

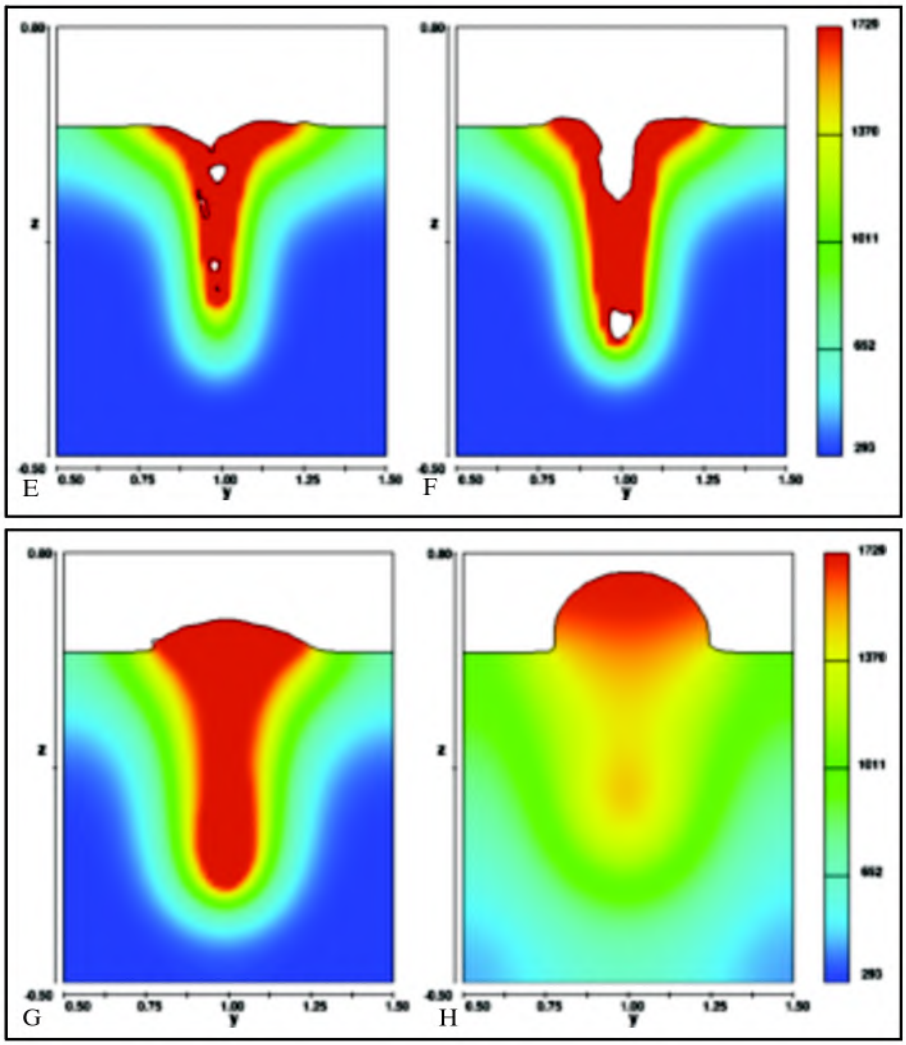

Fig. 5 — Temperature profiles of cross-sectioned front views in simulation result at postions, x=1.43. A — t=0.25 s; B — t=0.27 s; C — t=0.29 s; D — t=0.38 s; E — t=0.4 s; F — t=0.42 s; G — t=0.52 s; H — t=1.11 s.

be used in this simulation (Ref. 22).

$$P_R \cong 0.54 P_0 \exp\left(\Delta H_{LV} \frac{T - T_{LV}}{RTT_{LV}}\right) \qquad (16)$$

In Equation 15, μ_0 is the permeability in a vacuum. P_0 denotes the atmospheric pressure and ΔH_{LV} is the latent heat of vaporization. T, T_{LV}, and R indicate the surface temperature, liquid-vapor equilibrium temperature, and universal gas constant, respectively. The value 0.54 in Equation 15 is a factor that depends on the environmental pressure. This was also adopted in this research.

Heat source models and pressure models are prepared for application as boundary conditions. For the top surface, which is directly exposed to the heat sources of the arc and the laser, and for the arc and recoil pressure, the mathematical expressions are as follows:

$$K\frac{\partial T}{\partial n} = \eta_L q_L + \eta_A q_A - h_A\left(T - T_\infty\right) - \sigma_s \varepsilon_r \left(T^4 - T_\infty^4\right) - q_{vap} \qquad (17)$$

$$-P + 2\mu\frac{\partial V_n}{\partial n} = -P_R - P_A + \frac{\gamma}{R_c} \qquad (18)$$

In Equation 17, n denotes the normal component, K is the thermal conductivity, and T is the surface temperature. η denotes the heat input efficiency, i.e., the heat absorption rate, and the subscripts L and A indicate the laser and arc, respectively. The efficiency for the laser heat source is determined by the Fresnel reflection model and multiple reflections in the keyhole, which are discussed in later paragraphs. On the other hand, the efficiency of the arc is predetermined as 0.56. The heat input efficiency of the droplets was found to be 0.24 in this simulation; therefore, the total GMAW efficiency was set at 80%, which refers to Ref. 28. The third and fourth terms on the right side of this equation denote the heat losses caused by ambient air convection and heat radiation. Accordingly, h_A is the convection coefficient, which is 40 W/m² K here, and T_∞ is the temperature of the ambient air, set here as 293 K. σ_s, ε_r, and q_{vap} indicate the Stefan-Boltzmann constant, the emissivity, and the heat loss caused by vaporization, respectively. Equation 18 calculates the pressure boundary condition for the top surface including the surface tension in a flow. μ denotes the dynamic viscosity, γ and R_c indicate the surface tension coefficient and the radius of the surface curvature, respectively.

All of the other boundaries, such as the rear, front, and side, are set as continuous surfaces. This implies that the material exists continuously so the normal derivatives of all the properties at the boundary are equal to zero. The zero derivative condition is intended to represent a smooth continuation of the flow through the boundary.

In addition to the high power density of the laser, the main driving force that makes the keyhole deeper is the multiple reflections of the laser beam in the keyhole. If the laser is regarded as a bundle of ray beams, all of the rays coming into the keyhole experience multiple reflections on the wall and finally reach the bottom of the keyhole. These superposed rays inside the keyhole raise the total energy absorption and obtain a deeper penetration. In this research, the ray tracing technique is triggered on for every time step following to the self-evolved three-dimensional keyhole profile. Detailed descriptions can be found in an earlier published report by the author (Ref. 23).

The molten surface of the metal is regarded as specular in this paper; thus, it was deemed reasonable to adopt the Fresnel reflection model (Ref. 25), which is widely accepted for the calculation of laser absorption rate. Reflectivity R_f at the molten surface is mainly dependent on the angle between the incident ray and surface normal ϕ as follows, and the absorption rate η_f is then $1 - R_f$.

$$R_f = \frac{1}{2}\left(\frac{1+\left(1-\varepsilon\cos\phi\right)^2}{1+\left(1+\varepsilon\cos\phi\right)^2} + \frac{\varepsilon^2 - 2\varepsilon\cos\phi + 2\cos^2\phi}{\varepsilon^2 + 2\varepsilon\cos\phi + 2\cos^2\phi}\right) \qquad (19)$$

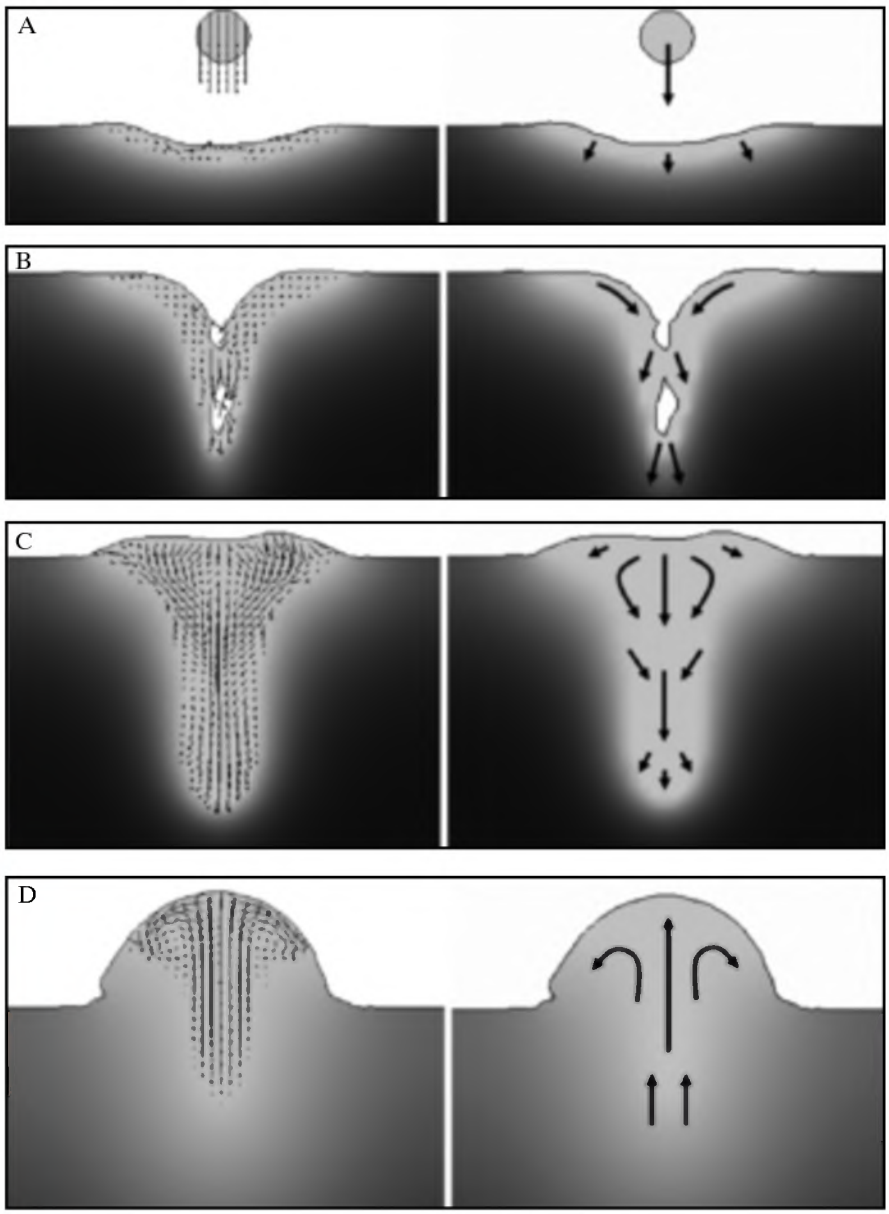

Fig. 6 — Flow patterns of simulation result in cross-sectioned front views at x=2.31. A— t=0.84 s; B — t=0.95 s; C — t=1.03 s; D — t=1.9 s.

$$\varepsilon^2 = \frac{2\varepsilon_2}{\varepsilon_1 + \left[\varepsilon_1^2 + \left(\sigma_{st}/\omega\varepsilon_0\right)^2\right]^{1/2}} \qquad (20)$$

The value of ε is related to the electrical conductance per unit depth of metal σ_{st}, and ε_1 and ε_2 denote the real part of the dielectric constants of metal and plasma, respectively. Additionally, ε_0 indicates the permittivity of a vacuum, and ω is one of the laser properties representing the angular frequency. The value ε is determined from the material properties and the laser type. For a CO_2 laser and a steel workpiece, this value is 0.08. However, it is also modifiable for several reasons. First, the temperature of the keyhole wall is at the boiling point, which could affect the Fresnel absorption. Moreover, the method used to calculate the Fresnel absorption is approximated, and the use of a large value of ε could offset the approximations (Ref. 25). Therefore, the value of ε can be determined by trial and error to fit the simulation result to the experimental result. The aim of this research is not to determine the proper coefficient; rather, the paper is purely focused on observing the fluidic phenomena achieved using a numerical method.

In addition to the gravitational force, another body force in the flow is the electromagnetic force induced by the arc current inside the workpiece. Simplified electromagnetic force in the pool is explained by the following equation set (Refs. 9, 26).

$$F_x = -\frac{\mu_m I^2}{4\pi^2 r_A^2 r}\exp\left(-\frac{r^2}{2r_A^2}\right) \times\left[1-\exp\left(-\frac{r^2}{2r_A^2}\right)\right]\left(1-\frac{z}{c}\right)^2\frac{x}{r} \qquad (21)$$

$$F_y = -\frac{\mu_m I^2}{4\pi^2 r_A^2 r}\exp\left(-\frac{r^2}{2r_A^2}\right) \times\left[1-\exp\left(-\frac{r^2}{2r_A^2}\right)\right]\left(1-\frac{z}{c}\right)^2\frac{y}{r} \qquad (22)$$

$$F_z = \frac{\mu_m I^2}{4\pi^2 r^2 c} \left[1-\exp\left(-\frac{r^2}{2r_A^2}\right)\right]^2\left(1-\frac{z}{c}\right) \qquad (23)$$

In these equations, μ_m is the magnetic permeability of the material, I is the arc current, and c is the thickness of the workpiece. For the coordinate value, x and y denote the distance from the arc position according to each axis, and z indicates the distance from the top of the workpiece along the z axis.

Results and Discussion

The material adopted for the simulations was ASTM A131 steel with a thickness of 10 mm. The analytic domain was set as 42 mm in length, 10 mm in width, and 13 mm in height including the void region of the top 3 mm for free-surface tracking. In the Cartesian coordinate system, the ranges of the domain are (2 mm, 44 mm) in the x axis, (5 mm, 1.5 mm) in the y axis, and (–0.5 mm, 0.8 mm) in the z axis, respectively. The inter-grid distance is equal to 0.1 mm along the three axes; consequently, there is a total of 2,860,000 element cells. The physical properties of the material and coefficients used in the simulation are shown in Table 1. It took 328 hours to complete the simulation.

Figure 1 shows a schematic diagram of the solution domain of the simulations. In this figure, the F value denotes the filled portion of the fluid (material) in a cell using the VOF method; i.e., F=1 indicates that the cell is fully filled with fluid, F=0 indicates that it is empty, and 0<F<1 signifies that it is partially filled. While the gas metal arc leads the welding process 3 mm ahead of the laser, the arc and laser power in this case is 2.5 kW (current 150 A and voltage 16.7 V) and 3.7 kW, respec-

tively, and the welding speed is set at 1 m/min. The instance of a 2-s GMA-laser hybrid welding process is simulated and analyzed.

In addition to the arc heat source model, it is necessary to determine the effect of droplets as a heat source in GMAW. Conventionally, droplets are treated as an additional surface heat flux with a Gaussian distribution when the free-surface tracking is not readily available. In this study, the droplets are assumed to be at a temperature 2400 K and are essentially generated to have the mass and momentum and to have fallen into the pool by the gravity and electromagnetic force. The diameter of the droplets is assumed to be equal to that of the electrode wire; consequently, the generation frequency 167 Hz is determined according to the wire feed rate of 8 m/min. The initial velocity of the droplet is assumed to have only the vertical (z-axis) component and its magnitude is 50 cm/s (Ref. 13).

Figure 2 shows three-dimensional perspective scenes of the simulation result. Droplets of welding wire are continuously generated in the void region and fall into the pool. It is observable that the surface of the molten pool is slightly dimpled due to the arc pressure in the figures. Directly behind the dimpled arc region, the keyhole opening is shown, resembling a cavity. Given that the distance between the arc and the laser is only 3 mm, the keyhole opening is located in the dimpled shape. Therefore, the keyhole and dimple are merged and can be observed as one large hole in a lateral cross-section plane near the top surface level of the workpiece. It is important to note that the shape of the free surface is maintained in a macroscopic view while the heat sources are moving forward. However, an unstable keyhole continuously repeats the generation and collapse process. Additionally, the inertia of the falling droplets causes the pool to oscillate. This is discussed in detail in the following paragraphs.

The solid and liquid regions and their boundaries are displayed in Fig. 3, which also shows the temperature profiles. In the series of figures, it is possible to observe the droplets generated above the workpiece as well as the dimpled shape at the arc position. Moreover, it is easy to compare the penetration depths of the GMA and laser welding processes. The difference is clearly distinct as the penetration depth of the GMA process does not exceed 1.5 mm while the depth of the keyhole is more than 6 mm. It is important that the free surface of the keyhole does not appear in these figures, not because the model is incorrect, but because the output file is not saved in a sufficient number of shot intervals. The results are saved every 10 ms. The keyhole is continuously repeating the generation and collapse process with a time interval

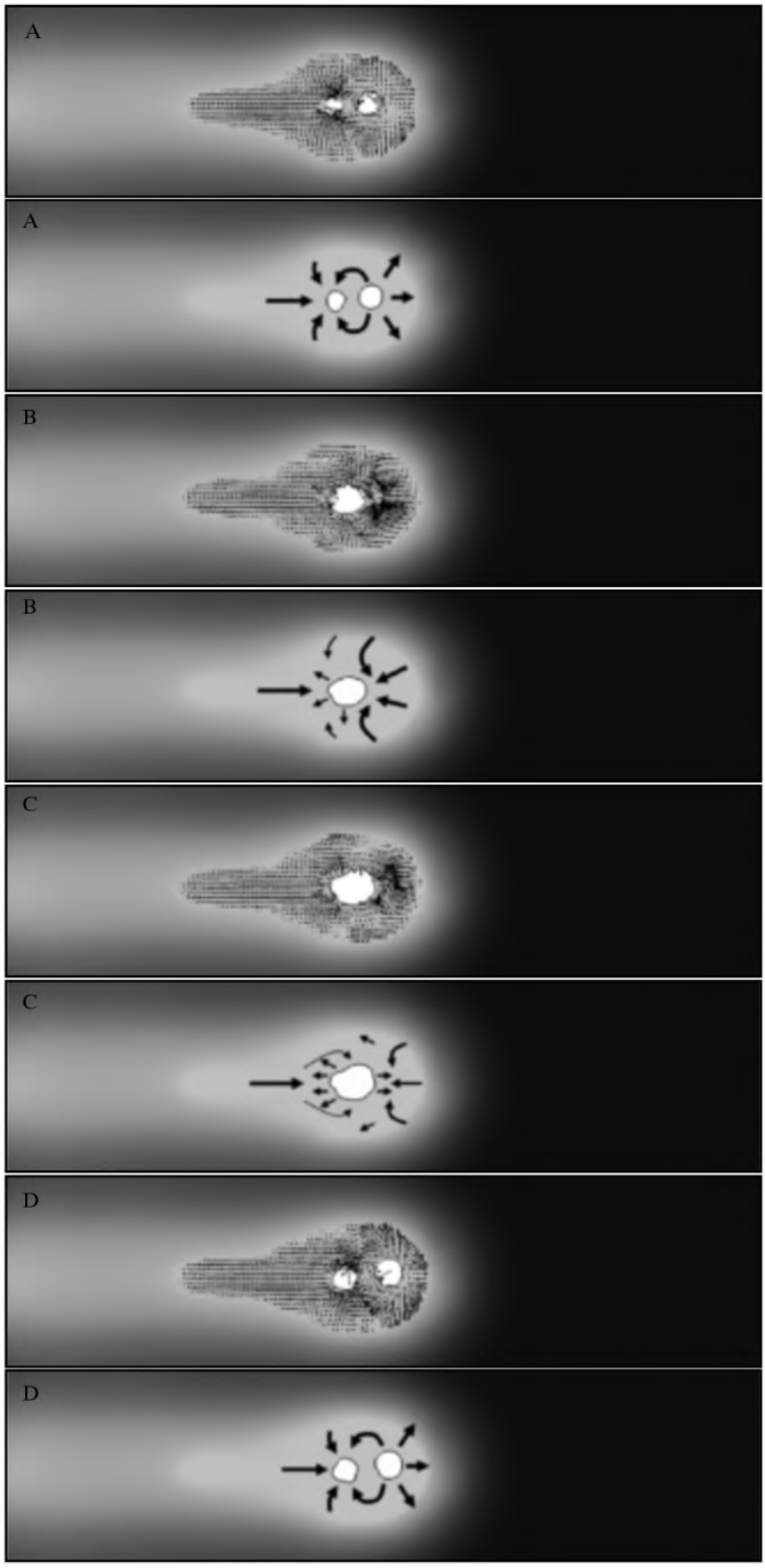

Fig. 7 — Flow patterns of the simulation result in cross-sectioned top views at z=0.47. A — t=1.03 s; B — t=1.04 s; C — t=1.05 s; D — t=1.06 s.

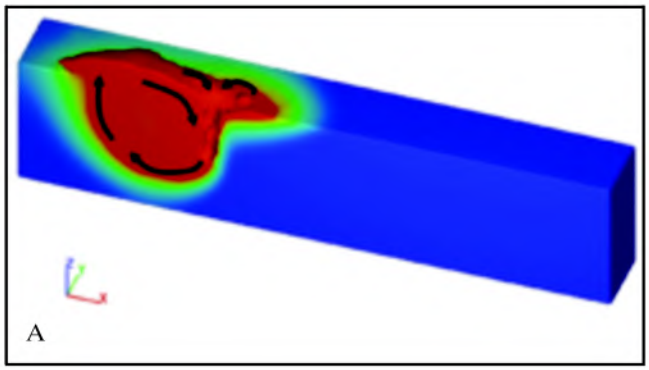

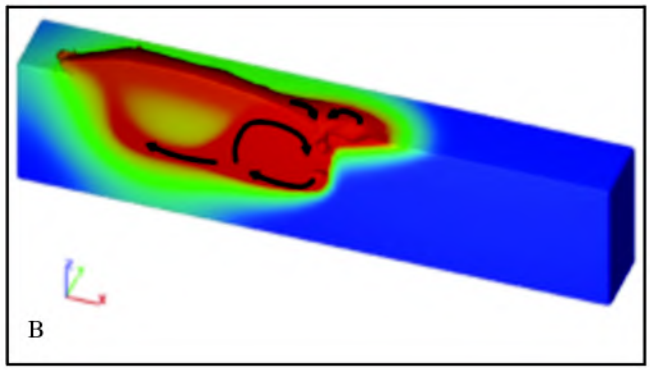

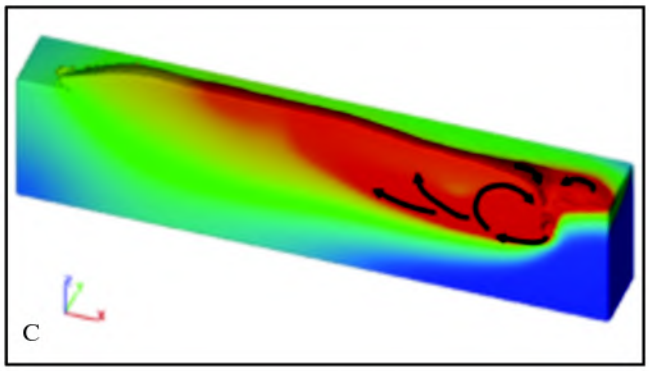

Fig. 8 — Flow patterns of simulation result in 3-D perspective views. A — t=0.53 s; B — t=1.0 s; C — t=1.96 s.

shorter than 10 ms; therefore, the free surface of the keyhole is not observed during every time step.

Nonetheless, the generation of the keyhole was fortuitously captured at 0.53 s, as seen in Fig. 4. These figures show the flow patterns of the molten pool. Figure 4A shows the moment of keyhole generation. There is a small amount of liquid metal in the front keyhole wall and the free surface of the keyhole is slightly inclined, as was shown in a previous report (Refs. 27, 29), as the laser is a moving heat source. Near the bottom of the keyhole, flow is downward due to the repulsive force caused by the recoil pressure. The molten flow reached the bottom at the solid/liquid boundary and is directed backward and is finally lifted up owing to the buoyancy. This circular pattern causes a vortex, as seen in the figures. The vortex serves to stir the pool to form an alloy. There is only one circular vortex at the beginning of the process as seen in Fig. 4A; however, while the heat sources are marching forward, the flow pattern becomes more complex as the root flow at the bottom is split into two main streams as shown in Fig. 4B. It ultimately branches out to three streams, as seen in Fig. 4C, but the circular vortex at the beginning is maintained and continues to move forward. The collapse of the keyhole begins from the middle of the walls, which can be deduced by analyzing Fig. 4A and C. In Fig. 4A, the flow vectors are directed to the center at the middle of the keyhole walls. With this tendency, a trapped bubble in the middle of the pool is observed for an instant in Fig. 4C due to the collapse of the keyhole.

Figure 5 shows a series of cross-sectioned front views. The sectioned plane is located at the position $x=1.43$, which is in the transverse middle range of the workpiece. This location was chosen to observe the entire welding process from melting to resolidification. As seen in the figures, the workpiece is melted by the pure arc first and the droplets are then added to the pool and cause the penetration to become somewhat deeper. Directly after the droplets transfer, the front keyhole walls begin to appear. In this section, it is observable that the penetration gradually deepens in the figures from 5D to 5F, which coincides with the fact the keyhole is slightly inclined, as mentioned in the previous paragraph. Trapped bubbles are also seen in the figures due to the collapse. After the simulation, there are no pores in the weldment, which can be expected owing to the trapped bubbles in the pool. It was believed that all of the bubbles escaped through the keyhole because the welding speed was not rapid enough to leave a bubble behind the keyhole. In Fig. 5G, all of the void regions are filled with liquid metal and the weld pool begins to solidify with upper streams, which finally form the top bead shape, as shown in Fig. 5H.

Flows in the front section are displayed in Fig. 6. A droplet is falling into the dimpled shape of the pool caused by the arc pressure with downward flow vectors — Fig. 6A. Directly after this action, a keyhole is generated with the downward flows at the liquid metal. A bubble is seen in Fig. 6B, which is not in the process of escaping, but is only pushed downward by the recoil pressure. However, it escapes from the pool, and that void region is filled with liquid metal and the cross-section bead shape is then determined, as seen in Fig. 6C. Flows at this moment are all downward as the circular returned flow from the bottom of the keyhole that was caused by the vortex reaches this position and forms the pool. All of the flows gradually disappear from the bottom due to the solidification, and finally the remaining flows that are pushed up shape the top bead, as in Fig. 6D.

Complexities of the flow patterns are shown in the cross-section top views — Fig. 7. The position of the section plane was selected as $z=0.47$ mm, which is only 3 mm below the top surface of the workpiece in order to observe both the keyhole and the arc dimple simultaneously. As shown in the figures, the keyhole and the arc dimple are continuously repeating the merge and separation action. It is important to note that when they are separated, flows around the arc dimple move toward the keyhole opening. However, the flows near the arc are outward and became more complex when they were merged. In the case of the separation, flow patterns toward the keyhole finally create a single hole and the outward patterns of the merged hole tend to separate the keyhole and the arc dimple. Due to this mechanism of flow patterns, the keyhole and arc dimple are repeatedly merged and separated. It can be derived that this phenomenon is repeated every 30 ms by analyzing the figures.

Figure 8 shows the three-dimensional flow patterns concluded from all of the procedures mentioned previously. Essentially, the pool has complex flow patterns. However, it is worth noting that the drawn mainstreams dominate the bead-shaping procedure. As seen here, the flows became more complicated while in the process of moving forward. The flow from the keyhole root is split into three

main streams as seen in the figure. However, one vortex induced by the keyhole phenomenon is maintained in spite of the complex circumstances.

Conclusions

A simulation model for the analysis of the molten pool in the laser-arc hybrid welding process is proposed and an analysis is achieved using the Flow-3D commercial package. The model consists of the three major governing equations of the continuity, momentum, and energy equations. Additionally, the VOF method is adopted to realize the tracking of the free surface of the pool. Physical phenomena of arc welding in the molten pool, such as the electromagnetic force, surface tension, and arc pressure are applied as the boundary conditions or the body force of the fluid. To obtain the keyhole dynamics via laser welding, the effect of multiple reflections in the keyhole is realized with a ray-tracing technique, which is suitable for the discrete grid cell system in the FVM and the VOF methods. In addition, the Fresnel reflection model is employed as an energy absorption mechanism for the laser beam on metal surfaces. The simulation results can be summarized as follows.

1) Due to the flow of the keyhole bottom, a vortex exists that mainly influences the shaping of the top bead.

2) Trapped bubbles are observed in the pool because keyhole collapse begins from the middle height of its depth.

3) The welding speed is not fast enough to leave the bubbles behind the keyhole; therefore, it is inferred that the trapped air escapes through the keyhole.

4) The keyhole and the arc dimple are continuously repeating the merge and separation process every 30 ms in a lateral cross-section at a height of 0.47 mm. However, these parameters are dependent on welding conditions, therefore will not remain the same for other conditions.

5) The width of the bead is determined mainly by the GMA heat source and the penetration depth is strongly influenced by the laser.

Acknowledgment

This work was supported by POSCO and Brain Korea 21 project.

References

1. Bicknell, A., Smith, J. S., and Lucas, J. 1994. Arc voltage sensor for monitoring of penetration in TIG welds. *IEE Proc. Sci. Meas. Tech.* 141: 513–520.

2. Kim, C. H., and Na, S. J. 2001. A study of an arc sensor model for gas metal arc welding with rotating arc Part 1: Dynamic simulation of wire melting. *Proc. Institution of Mechanical Engineers. Part B, Journal of Engineering Manufacture* 215: 1271–1280.

3. Kim, C. H., and Na, S. J. 2001. A study of an arc sensor model for gas metal arc welding with rotating arc Part 2: Simulation of an arc sensor in mechanically rotating gas metal arc welding. *Proc. Institution of Mechanical Engineers. Part B, Journal of Engineering Manufacture* 215: 1281–1288.

4. Wu, C. S., Gao, J. Q., Liu, X. F., and Zhao, Y. H. 2002. Vision-based measurement of weld pool geometry in constant-current gas tungsten arc welding. *Proc. Institution of Mechanical Engineers. Part B, Journal of Engineering Manufacture* 217: 879–882.

5. Zhang, Y. M., Wu, L., Chen, D. H., and Walcott, B. L. 1993. Determining joint penetration in GTAW with vision sensing of weld face geometry. *Welding Journal* 72(10): 463-s to 469-s.

6. Fujinaga, S., Takenaka, H., Narikiyo, T., and Katayama, S. 1998. Observation of keyhole behavior during high power YAG laser welding with microfocused X-ray transmission imaging system. *Laser Materials Processing Conference*. 158–167.

7. Matsunawa, A., Seto, N., Mizutani, M., and Katayama, S. 1999. X-ray observation of keyhole dynamics in high power laser welding. *International Welding Conference; (IWC 99) On Welding & Allied Technology, "Challenges in 21st century."* pp. 46–53.

8. Kim, I. S., and Basu, A. 1998. A mathematical model of heat transfer and fluid flow in the gas metal arc welding process. *Journal of Materials Processing Technology* 77: 17–24.

9. Tsao, K. C., and Wu, C. S. 1988. Fluid flow and heat transfer in GMA weld pools. *Welding Journal* 67(3): 70-s to 75-s.

10. Ohring, S., and Lugt, H. J. 1999. Numerical simulation of a time-dependent 3-D GMA weld pool due to a moving arc. *Welding Journal* 78(12): 416-s to 424-s.

11. Kim, C. H., Zhang, W., and DebRoy, T. 2003. Modeling of temperature field and solidified surface profile during gas metal arc fillet welding. *Journal of Applied Physics* 94: 2667–2679.

12. Wang, Y., and Tsai, H. L. 2001. Impingement of filler droplets and weld pool dynamics during gas meal arc welding process. *International Journal of Heat and Mass Transfer* 44: 2067–2080.

13. Cao, Z., Yang, Z., and Chen, X. L. 2004. Three-dimensional simulation of transient GMA weld pool with free surface. *Welding Journal* 85: 169-s to 176-s.

14. Mahrle, A., and Schmidt, J. 2002. The influence of fluid flow phenomena on the laser beam welding process. *International Journal of Heat and Fluid Flow* 23: 288–297.

15. Zhang, W. H., Zhou, J., and Tsai, H. L. 2003. Numerical modeling of keyhole dynamics in laser welding. *Proc. of SPIE* 4831: 180–185.

16. Ki, H., Mohanty, P. S., and Majumder, J. 2002. Modeling of laser keyhole welding: Part I. Mathematical modeling, numerical methodology, role of recoil pressure, multiple reflections, and free surface evolution. *Metallurgical and Materials Transactions A* 33A: 1817–1830.

17. Ki, H., Mohanty, P. S., and Majumder, J. 2002. Modeling of laser keyhole welding: Part II. Simulation of keyhole evolution, velocity, temperature profile, and experimental verification. *Metallurgical and Materials Transactions A* 33A: 1831–1842.

18. Ki, H., Mohanty, P. S., and Majumder, J. 2002. Multiple reflections and its influence on keyhole evolution. *Journal of Laser Applications* 14: 39–45.

19. Hirt, C. W., and Sicilian, J. M. 1985. A porosity technique for the definition of obstacles in rectangular cell meshes. *Proc. Fourth International Conf. Ship Hydro.*, National Academy of Science, Washington, D.C., September.

20. Hirt, C. W., and Nichols, B. D. 1981. Volume of fluid method for the dynamics of free boundaries. *Journal of Computational Physics* 39: 201–225.

21. Cho, Y. T. 2005. A study on the analysis and monitoring of plasma in laser arc hybrid welding. PhD thesis. KAIST. pp. 21, 22.

22. Lee, J. Y., Ko, S. H., Farson, D. F., and Yoo, C. D. 2002. Mechanism of keyhole formation and stability in stationary laser welding. *Journal of Physics D: Applied Physics* 35: 1570–1576.

23. Cho, J. H., and Na, S. J. 2006. Implementation of real-time multiple reflection and Fresnel absorption of laser beam in keyhole. *Journal of Physics D: Applied Physics* 39: 5372–5378.

24. Cho, J. H., and Na, S. J. 2006. Three-dimensional analysis of molten pool in laser-GMA hybrid welding. *Proc. of LAMP 2006*, #06-183.

25. Ducharme, R., Williams, K., Kapadia, P., Dowden, J., Steen, B., and Glowacki, M. 1994. The laser welding of thin metal sheets: An integrated keyhole and weld pool model with supporting experiments. *Journal of Physics D: Applied Physics* 27: 1619–1627.

26. Kumar, A., and DebRoy, T. 2003. Calculation of three-dimensional electromagnetic force field during arc welding. *Journal of Applied Physics* 94: 1267–1277.

27. Matsunawa, A., and Katayama, S. 2002. Keyhole instability and its relation to porosity formation in high power laser welding. *Proc. Joining of Advanced and Specialty Materials*, pp. 8–15.

28. DuPont, J. N., and Marder, A. R. 1995. Thermal efficiency of arc welding process. *Welding Journal* 74(12): 406-s to 416-s.

29. Fujinaga, S., Takenaka, H., Narikiyo, T., Katayama, S., and Matsunawa A. 2000. Direct observation of keyhole behavior during pulse modulated high-power Nd:YAG laser irradiation. *Journal of Physics D: Applied Physics* 33: 492–497.